Anomalous Nernst Effect in Epitaxial $L1_0$ $FePd_{1-x}Pt_x$ Alloy Films: Berry Curvature and Thermal Spin Current

Zhong Shi,[1,*] Shi-Jie Xu,[1] Li Ma,[2] Shi-Ming Zhou,[1] and Guang-Yu Guo[3,4,†]

[1] *Shanghai Key Laboratory of Special Artificial Microstructure and Pohl Institute of Solid State Physics and School of Physics Science and Engineering, Tongji University, Shanghai 200092, China*

[2] *School of Materials Science and Engineering, Xi'an University of Technology, Xi'an 710048, China*

[3] *Department of Physics, National Taiwan University, Taipei 10617, Taiwan*

[4] *Physics Division, National Center for Theoretical Sciences, Hsinchu 30013, Taiwan*

(Received 28 January 2020; revised manuscript received 22 March 2020; accepted 16 April 2020; published 19 May 2020; corrected 25 September 2020)

Anomalous Nernst effect in epitaxially grown $L1_0$-ordered $FePd_{1-x}Pt_x$ alloy films is systematically investigated both experimentally and theoretically. It is found that the anomalous Nernst coefficient and anomalous Hall resistivity both increase monotonically with the increase of Pt composition. By subtracting the Seebeck contribution, the anomalous Nernst conductivity (α_{xy}^A) is obtained. By comparison with first-principles Berry-phase-theory calculations, it is interesting to find that the anomalous Nernst conductivity is dominated by the intrinsic contribution from heavy metal Pt-Pd with large spin-orbit coupling strength. Moreover, the first-principles calculations also predict a large spin Nernst counductivity for both $L1_0$-ordered FePd and FePt. Thus, the present results may shed light in searching materials with large thermally driven Hall and spin currents.

DOI: 10.1103/PhysRevApplied.13.054044

I. INTRODUCTION

Spin caloritronics has opened a unique field in spintronics to study and manipulate the interplay between spin and heat current in electronic systems [1–3]. The investigation of thermoelectric effects in magnetic materials provides a potential way to develop thermal management technologies for information industry. Among the emerging thermoelectric effects such as spin Seebeck effect and spin Peltier effect [4,5], the anomalous Nernst effect (ANE) has received intensive studies in the past decades [6–18]. It is dated back to 1886, when Walther Nernst and Albert von Ettingshausen first carried out the experiment by utilizing an entropy flow in a ferromagnetic material along its longitudinal direction. Therefore, an electric voltage (anomalous Nernst voltage, V_{ANE}) was generated in the transverse direction, which is perpendicular to both the thermal gradient (∇T) and the out-of-plane magnetization (M_z). The ANE shares the same configuration as anomalous Hall effect (AHE) despite the electric potential in ANE is replaced by thermal gradient ∇T. Analogous to anomalous Hall coefficient (R_s), the anomalous Nernst coefficient (Q_s) is defined as

$$Q_s = \frac{E_{\mathrm{ANE}}}{4\pi M_s \nabla T}, \tag{1}$$

where E_{ANE} and M_s are the anomalous Nernst electric field and saturation magnetization, respectively. When temperature gradient is restricted along x direction, ∇T can be expressed as $\partial_x T$ with a simple boundary condition $\partial_y T = 0$. On the other hand, the longitudinal and transverse Seebeck coefficients are expressed as

$$\begin{aligned} S_{xx} &= \frac{E_x}{\partial_x T}, \\ S_{xy} &= -\frac{E_y}{\partial_x T}, \end{aligned} \tag{2}$$

where E_x (or E_{SBK}) is the Seebeck electric field along x direction and E_y is the anomalous Nernst electric field along y direction. In linear response theory of the thermoelectric dissipation scenario, with the presence of a weak electric field and a small thermal gradient, the expression of the charge current $\mathbf{j}$ reads as [10]

$$\mathbf{j} = \hat{\sigma} \cdot \mathbf{E} - \hat{\alpha} \cdot \nabla \mathbf{T}, \tag{3}$$

where the electric conductivity tensor and thermoelectric conductivity tensor are denoted by $\hat{\sigma}$ and $\hat{\alpha}$, respectively. In an open-circuit condition, and neglecting the ordinary Hall and ordinary Nernst effect in the ferromagnet, one can get the following equation:

$$4\pi M_s Q_s = \rho_{xx}(\alpha_{xy}^A - S_{xx}\sigma_{xy}^A) \tag{4}$$

*shizhong@tongji.edu.cn
†gyguo@phys.ntu.edu.tw

and thus

$$\alpha_{xy}^{A} = \frac{4\pi M_s Q_s}{\rho_{xx}} + S_{xx}\sigma_{xy}^{A}, \tag{5}$$

where the ρ_{xx} is the longitudinal electric resistivity, σ_{xy}^{A} and α_{xy}^{A} are the anomalous Hall conductivity (AHC) and anomalous Nernst conductivity (ANC), respectively [10]. Furthermore, one can find that E_y is equal to E_{ANE} in such a condition, and the conversion between S_{xy} and Q_s can be obtained as $S_{xy} = -4\pi M_s Q_s$ thereafter [7]. Thus, the anomalous Nernst coefficient Q_s has mixed contributions of electrical anomalous Hall effect and entropy flow induced by thermoelectrical anomalous Nernst effect. In this scenario, the Seebeck effect can provide E_x without electric current source. The first term in Eq. (4) corresponds to the transverse thermoelectric current, and the latter term is attributed to the anomalous Hall current caused by the Seebeck effect. In order to disentangle the value of α_{xy}^{A} in the ferromagnet, both the AHE and ANE must be measured on the same sample. The detailed derivations and results are provided within the Supplemental Material [19]. The anomalous Nernst conductivity, also known as the anomalous transverse thermoelectric conductivity, is a key parameter to quantify the ANE. The α_{xy}^{A} can be related to the energy (E) derivative of the AHC (σ_{xy}^{A}) at the Fermi surface via the well-known Mott relations [20,21],

$$\alpha_{xy}^{A} = -\frac{\pi^2}{3}\frac{k_B^2 T}{e}\sigma_{xy}^{A}(\mu)', \tag{6}$$

where μ is the chemical potential and k_B is the Boltzmann constant [7,10,11]. In principle, the α_{xy}^{A} in ANE can provide more information on the origin of off-diagonal transportation behavior, since it reflects the interconverse of spin, charge, and entropy flow in magnetic materials.

$L1_0$-ordered FePt, has promising applications to high-performance ultrahigh-density magnetic recording media because of its large uniaxial magnetic anisotropy, which is due to the strong spin-orbit coupling (SOC) strength (ξ) in the alloy [22,23]. Meanwhile, the layered epitaxial growth of iron and platinum atoms gives further asymmetry in structure, which is believed to have larger anomalous Hall conductivity compared to bulk iron or disordered FePt. Furthermore, as a model system, isoelectronic $L1_0$-ordered $FePd_{1-x}Pt_x$ ternary alloy films are ideal candidates to study the off-diagonal conductivity because ξ could be smoothly increased several times by gradually replacing the Pd atoms with the Pt atoms while keeping other physical parameters such as crystalline structure and lattice constants almost unchanged. Therefore, extensive studies of AHE were carried out in $L1_0$ $FePd_{1-x}Pt_x$ with x ranging from 0 to 1 in order to establish an overall physical picture on the SOC dependence of the AHC [24,25]. Recently, the intrinsic anomalous Hall conductivity [σ_{xy}^{A}(int)] in $L1_0$ $FePd_{1-x}Pt_x$ is well explicated by the language of Berry curvature [20,26,27], which can be formulated as an integration of the Berry curvature of all the occupied bands over the *entire Brillouin zone* [11,24]. However, unlike its counterpart, the intrinsic anomalous Nernst conductivity [α_{xy}^{A}(int)] relies more on the Berry phase acquired by the moving particles *on the Fermi surface* [11,14,28]. Thus, the magnitude of α_{xy}^{A} is more sensitive to the band structure close to the Fermi surface. Nevertheless, although $L1_0$-ordered $FePd_{1-x}Pt_x$ has received intensive investigations on its AHE properties, only one research group has reported on the anomalous Nernst effect [8,13], of which only the anomalous Nernst coefficient Q_s is obtained. The experimental data of α_{xy}^{A} are still lacking for $L1_0$ $FePd_{1-x}Pt_x$ with x changing.

In this paper, we present a study of the anomalous Nernst effect along with the anomalous Hall effect in high-quality $L1_0$-ordered $FePd_{1-x}Pt_x$ epitaxial films with varying Pd-Pt ratio. S_{xx} is measured simultaneously in order to derive the magnitude of α_{xy}^{A}. It is found that α_{xy}^{A} and σ_{xy}^{A} for $L1_0$-ordered $FePd_{1-x}Pt_x$ alloys can be monotonically tuned by changing the composition of Pt. The spin-orbit coupling coefficient ξ and the ANC have the same trend with the change of Pt atomic composition. The *ab initio* calculations show that the trend of α_{xy}^{A} in $L1_0$-ordered $FePd_{1-x}Pt_x$ alloys can be related to the unique Berry curvature distribution in their band structures. It is also noted that the results of anomalous Nernst effect were reported in noncollinear antiferromagnet Mn_3Sn recently [14,15], which shows the correlation between the large α_{xy}^{A} and the particular Berry curvature in such a chiral antiferromagnet [29]. Furthermore, the spin Hall effect and anomalous Hall effect share the similar mechanism, which are simply the sum and difference of the spin-up and spin-down transverse currents, respectively [30–32]. Since the spin Nernst effect and anomalous Nernst effect are connected to each other in a similar way, it is believed that the present study on the anomalous Nernst effect will also help to better understand the property of the intriguing spin Nernst effect, observed very recently [33,34].

II. EXPERIMENTS AND CALCULATION

The $L1_0$-ordered $FePd_{1-x}Pt_x$ alloy films with different Pt atomic composition x are deposited on MgO substrates by dc magnetron sputtering. The detailed fabrication process is described elsewhere [24]. The microstructure is characterized by XRD by a Bruker D8 diffractometer with five-axis configuration and Cu Kα ($\lambda = 0.1542$ nm). The film thickness and the surface roughness are characterized by x-ray reflectivity (XRR). The thicknesses of the films investigated in this work are all about 20 nm. The epitaxial growth of films is further confirmed by the x-ray pole figures. The chemical composition is characterized by energy dispersive x-ray spectroscopy (EDX). During the AHE and ANE measurements, an external magnetic field

is set normal to the film plane. The longitudinal resistivity ρ_{xx} and the transverse resistivity ρ_{xy} are measured at room temperature by a physical property measurement system (Quantum Design PPMS-9 T system) with standard Hall-bar patterns. Magnetic hysteresis loops are measured by VSM. For the thermoelectric measurement, two edges of each sample are contacted to two disparate copper plates. In order to establish a stable thermal gradient ∇T, one copper plate is heated by a high-precision resistor, and another one is proximate to and cooled by a large heat sink. The longitudinal and transverse thermoelectric voltage, which corresponds to the Seebeck and Nernst voltage are simultaneously recorded by Keithley 2182A nanovoltmeters, respectively (see Supplemental Material [19]).

The intrinsic anomalous Hall conductivity and anomalous Nernst conductivity are calculated based on the elegant Berry-phase formalism [20]. The intrinsic AHC arises as a result of an additional term in the group velocity of Bloch electrons:

$$\dot{\mathbf{r}} = \frac{1}{\hbar}\frac{\partial \epsilon_{n(\mathbf{k})}}{\partial \mathbf{k}} + \dot{\mathbf{k}} \times \Omega_n(\mathbf{k}).$$

In the presence of an electric field $\mathbf{E}$ and a magnetic field $\mathbf{B}$, $\hbar\dot{\mathbf{k}} = -e\mathbf{E} - e\dot{\mathbf{r}} \times \mathbf{B}$, with

$$\Omega_n(\mathbf{k}) = -\sum_{n' \neq n} \frac{2\,\mathrm{Im}\left[\langle \mathbf{k}n|v_i|\mathbf{k}n'\rangle\langle \mathbf{k}n'|v_j|\mathbf{k}n\rangle\right]}{(\epsilon_{\mathbf{k}n} - \epsilon_{\mathbf{k}n'})^2}.$$

Here, $\Omega_n(\mathbf{k})$ is the Berry curvature for the nth band at $\mathbf{k}$. Starting from this, the intrinsic AHC can be written as [11,20,29]

$$\sigma_{xy}^{A}(\mathrm{int}) = -\frac{e^2}{\hbar}\sum_n \int_{\mathrm{BZ}} \frac{d\mathbf{k}}{(2\pi)^3} f_{\mathbf{k}n}\Omega_n(\mathbf{k}), \tag{7}$$

where $f_{\mathbf{k}n}$ is the Fermi distribution function. The related intrinsic ANC is given by [11,20,29]

$$\alpha_{xy}^{A}(\mathrm{int}) = \frac{1}{T}\frac{e}{\hbar}\sum_n \int_{\mathrm{BZ}} \frac{d\mathbf{k}}{(2\pi)^3}\Omega_n^z(\mathbf{k}) \times \left\{(\epsilon_{\mathbf{k}n} - \mu) f_{\mathbf{k}n} + k_B T \ln\left[1 + e^{-\beta(\epsilon_{\mathbf{k}n}-\mu)}\right]\right\}. \tag{8}$$

Since both the intrinsic contributions of anomalous Nernst effect and anomalous Hall effect are caused by the spin-orbit coupling, first-principles calculations should be considered based on a relativistic band theory. Therefore, we perform self-consistent band-structure calculations by using the fully relativistic linear muffin-tin orbital method [35,36]. The calculations are based on the density-functional theory (DFT) with the generalized gradient approximation (GGA) in the form of Perdew-Burke-Ernzerhof [37]. To obtain accurate anomalous Hall conductivities, a dense k-point mesh is needed [11,29]. Therefore, a very fine k-point mesh of about 3×10^6 k-points in the first Brillouin zone is used. Test calculations using more k points in the first Brillouin zone indicate that the calculated intrinsic AHC converges to within 2%.

III. RESULTS AND DISCUSSION

A. Structure and characterization

Figures 1(a) and 1(b) present typical XRR and XRD spectra of the $L1_0$-ordered $FePd_{1-x}Pt_x$ films, respectively. Kiessig fringes of all $FePd_{1-x}Pt_x$ films are observed in a wide angular region. By fitting the reflected amplitude of the x ray, the thickness of films is about 20 nm, and

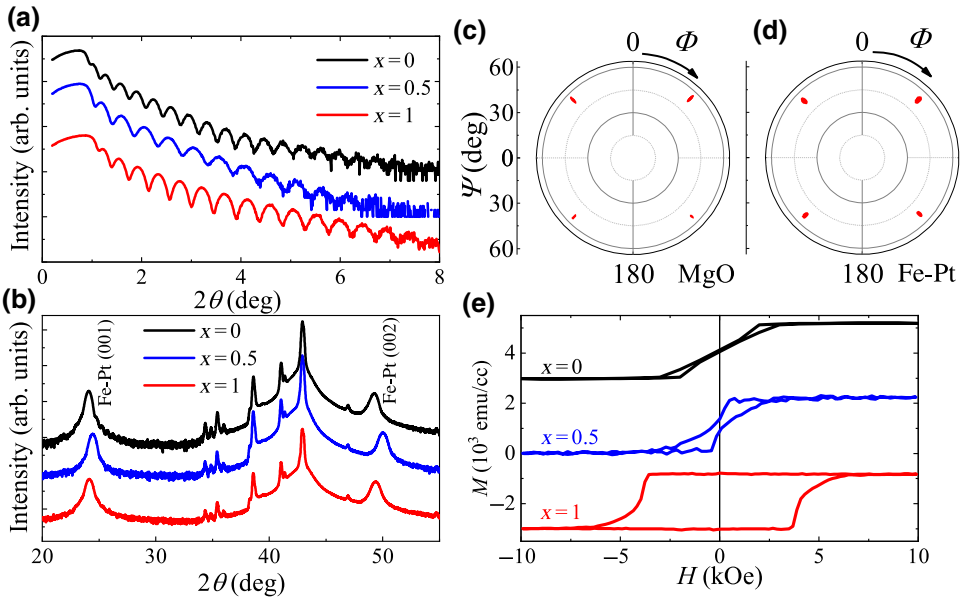

FIG. 1. (a) Typical XRR curves and (b) XRD diffractogram of $L1_0$-ordered $FePd_{1-x}Pt_x$ films with different Pt composition x, and (e) magnetic hysteresis loops for the corresponding films as well as (c) x-ray pole figures of MgO substrates and (d) 20-nm-thick $L1_0$-ordered FePt film along the [111] direction with $2\theta = 41.05°$ and 36.94°, respectively. For clarity, the curves in (a), (b), and (e) are vertically shifted.

the film surface roughness, as the standard deviation of the Fresnel coefficient, is found to be in the region of $0.3 \sim 0.5$ nm, mainly following the surface roughness of the commercial MgO substrates. For $FePd_{1-x}Pt_x$ films on MgO(001), two diffraction peaks near $2\theta = 24°$ and 49° correspond to the $FePd_{1-x}Pt_x$ (001) superlattice and (002) peaks, respectively, as shown in Fig. 1(b). The diffraction peak of (001) superlattice indicates the establishment of the long-range chemical ordering. The intensity of the (001) diffraction peak increases with the Pt composition x. This is because the atomic scattering factor of Pt is larger than that of Pd. Therefore, the more the alloy contains Pt, the larger the geometrical factor and scattering intensity are. The ordering parameter of all samples is around 0.9 ± 0.10 by comparing the intensity of (001) and (002) peaks [38]. Typical pole figures for the (111) plane of MgO(001) substrate and $L1_0$-ordered FePt ($x = 1$) are shown in Figs. 1(c) and 1(d). The poles at $2\theta = 45°$, 135°, 225°, and 315° represent the fourfold symmetry of film, further proving the high quality of epitaxial growth for $L1_0$-ordered $FePd_{1-x}Pt_x$ films on MgO(001) substrates. The perpendicular magnetic anisotropy of the $L1_0$-ordered $FePd_{1-x}Pt_x$ films could be tuned by varying x continuously. As shown in Fig. 1(e), the film has greater coercivity as x increases. As the saturation magnetization (M_s) is dominated by the iron part, M_s for all the samples does not change much and is about 1100 emu/cm^3, which is consistent with previous reports [24,25]. Typically, the measured M_s for $L1_0$ FePd ($x = 0$) and $L1_0$ FePt ($x = 1$) are 1012 and 1025 emu/cm^3, corresponding to 2.99 and 3.02 μ_B per formula unit, approximately [39,40].

B. Anomalous Nernst conductivity versus Pt concentration

The thermoelectric measurement setup with $L1_0$-ordered $FePd_{1-x}Pt_x$ films on MgO is shown in Fig. 2(a). A schematic illustration is also provided to display the spatial relationship between entropy flow, magnetic field, and electric field, as shown in Fig. S1 within the Supplemental Material [19]. In this work, entropy flow is applied in x direction and the external magnetic field H is along z direction, normal to the film plane. For the ANE measurement, varying magnitude of thermal gradient is realized by applying different power to the resistor heater next to the right side of the sample, while the left side is kept at room temperature by a large air-cooled copper plate as a heat sink, as shown in Fig. 2(a). The temperature gradient is read by thermometers, and further determined by the change of resistance of two pairs on Hall bar (for details about the ANE measurement, see the Supplemental Material [19]). Figure 2(b) displays two representative sets of the transverse thermoelectric voltage loop measured at different heating currents for the $L1_0$ FePt film. All the curves show a hysteresis looplike shape. In ferromagnetic materials, V_{ANE} is usually obtained after subtracting the linear ordinary Nernst voltage. The value of V_{ANE} is taken as half of the difference between V_{ANE+} and V_{ANE-}, i.e., $V_{ANE} = (V_{ANE+} - V_{ANE-})/2$, where the V_{ANE+} and V_{ANE-} are extrapolated from positive and negative high magnetic fields to zero magnetic field. A linear $\partial_x T$ dependence of E_{ANE} is found for all samples investigated in this work as shown in Fig. 2(c), which can be understood by Eq. (1). The slope of E_{ANE} over $\partial_x T$ is proportional to Q_s,

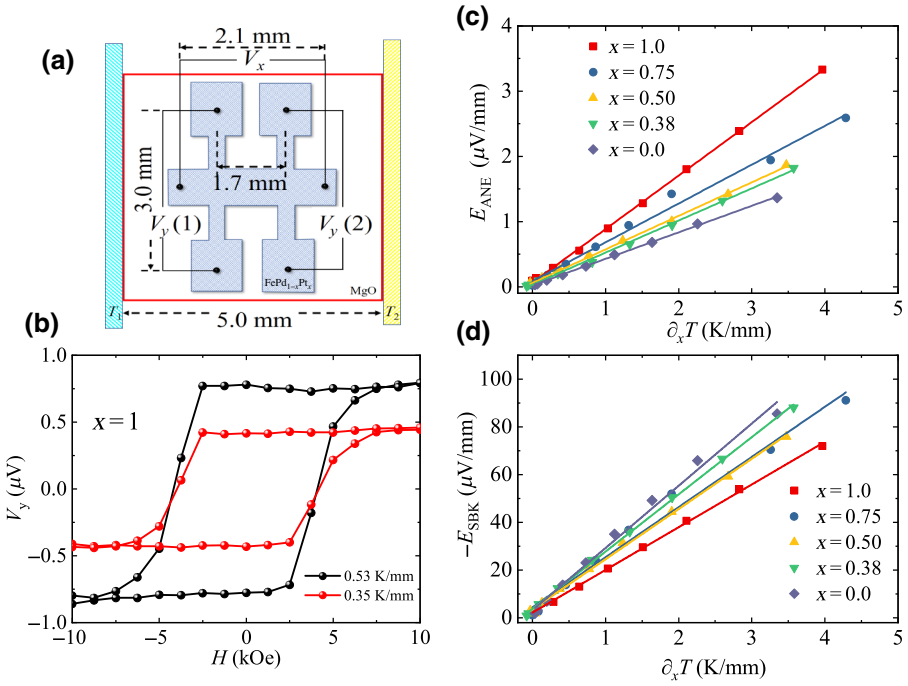

FIG. 2. (a) Sketch of the thermoelectric measurement geometry. The patterned $FePd_{1-x}Pt_x$ film is grown on the MgO substrate. Two copper plates are attached to the MgO substrate. The dimensions are indicated in the figure. (b) Typical curves of transverse thermoelectric voltage (V_y) versus magnetic field (H) for the FePt film. The black and red curves denote the results with $\partial_x T = 0.53$ K/mm and $\partial_x T = 0.35$ K/mm, respectively. The curves are vertically centered for clarification. Anomalous Nernst electric field (c) and Seebeck electric field (d) as a function of temperature gradient. The solid lines in (c) and (d) show the linear fitting results. All data are taken at room temperature.

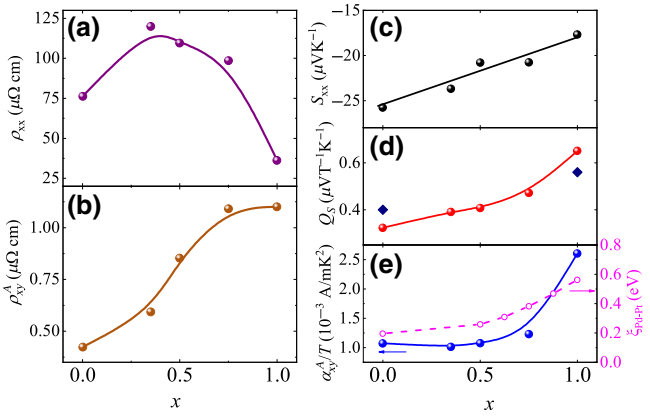

FIG. 3. (a) ρ_{xx} and (b) ρ^A_{xy} as a function of the Pt concentration x. (c) S_{xx}, (d) Q_s, and (e) α^A_{xy}/T and $\xi_{\text{Pd-Pt}}$ dependence on the Pt concentration x. The solid line in (c) shows the linear fitting result. Solid lines in (a), (b), (d), and (e) are guides to the eye only. The two diamond symbols in (d) are the experimental results by Hasegawa *et al.* [13].

and keeps ascending monotonically with increasing Pt concentration. Furthermore, the longitudinal Seebeck electric field of $L1_0$ $FePd_{1-x}Pt_x$ films is also recorded simultaneously, as shown in Fig. 2(d), of which the slope represents longitudinal Seebeck coefficient S_{xx}. The E_{SBK} of all samples have negative values in the whole x range, leading to a negative slope S_{xx}. The fact of negative S_{xx} indicates that longitudinal thermoelectric conversion in $FePd_{1-x}Pt_x$ is generally dominated by electronic charge carrier diffusion, which tends to push electrons towards the cold side of the material until a compensating voltage has been built up. Thus, the following discussions of AHC and ANC are both in the frame of electronic transport in $L1_0$-ordered $FePd_{1-x}Pt_x$ films.

To investigate the relationship between the ANC and AHC, we compare the electric resistivity and thermoelectric conductivity in Fig. 3. Firstly, ρ_{xx} and anomalous Hall resistivity ρ^A_{xy} from the anomalous Hall effect measurement, are shown in Figs. 3(a) and 3(b). The ρ_{xx} changes nonmonotonically with alloy composition and approaches a maximum close to $x = 0.5$, which has also been observed previously [24]. This can be attributed mainly to the nonmonotonic variation of defect concentration due to introducing Pt atoms into Pd sites, or may arise from the artifact that the Pd-Pt site disorder, and the scattering reaches the maximum at intermediate x. Secondly, the ρ^A_{xy} rises quickly with increasing x and approaches a plateau after $x > 0.75$. The results are consistent with previous studies [24,25]. It implies that in the ordered alloys studied here, the intrinsic contribution from spin-orbit coupling may play a major role in the anomalous Hall resistivity, as the spin-orbit coupling strength keeps increasing when Pt atoms substitute Pd atoms in $FePd_{1-x}Pt_x$, compared to the extrinsic contributions from the impurity scattering. In particular, the intrinsic contribution may overwhelm the extrinsic contribution with high Pt concentration. The anomalous Hall conductivity is derived by the relation of $\sigma^A_{xy} = \rho^A_{xy}/\rho^2_{xx}$. The composition dependence of longitudinal Seebeck coefficient S_{xx} and anomalous Nernst coefficient Q_s are shown in Figs. 3(c) and 3(d), respectively. As mentioned above, all the S_{xx} represent negative values, and show a linear decay as a function of x. In the semiclassical model, the Seebeck coefficient for metals can be simply expressed as $S_{xx} \approx (k_B/e)(k_BT/E_F)$, where E_F is the Fermi energy. The monotonic reduction of S_{xx} indicates a smooth variation of the band structure from FePd to FePt. As for comparison, S_{xx} of bulk Pd and Pt is about -10.7 and -5.3 μVK^{-1} at room temperature [41], respectively. On the other hand, the value of Q_s increases monotonically from 0.32 (at the FePd site) to 0.65 μVT^{-1}K^{-1} (at the FePt site), when x changes from 0 to 1, which is close to the value of Q_s reported by Hasegawa *et al.*, e.g., $Q_s = 0.40$ for $L1_0$ FePd and 0.55 for $L1_0$ FePt at room temperature, respectively [13], as shown in Table I.

Based on the AHE and ANE results of electric resistivity and thermoelectric coefficient, the anomalous Nernst conductivity α^A_{xy} can be derived from Eq. (5), while the anomalous Hall angle θ_H is small. The x dependence of α^A_{xy}/T is shown in Fig. 3(e) at $T = 300$ K. Firstly, the α^A_{xy}/T of $L1_0$ $FePd_{1-x}Pt_x$ increases almost monotonically with the Pt concentration, from 1.07×10^{-3} for FePd ($x = 0$) to 2.61×10^{-3} Am^{-1} K^{-2} for FePt ($x = 1$), which demonstrates that the ANC in the $FePd_{1-x}Pt_x$ ternary alloys can be engineered by chemical composition tuning. Secondly, the sign of $S_{xx}\sigma^A_{xy}$ is negative, opposite to the sign of the

TABLE I. Experimental Seebeck coefficient [S_{xx} (μVK^{-1})], anomalous Nernst coefficient [Q_s (μVT^{-1}K^{-1})], anomalous term of transverse Seebeck coefficient [S^A_{xy} (μVK^{-1})], anomalous Nernst angle [$|\theta_{\text{AN}}|$], and anomalous Nernst conductivity [α^A_{xy}/T ($\times 10^{-3}$ Am^{-1} K^{-2})] of $L1_0$ FePd and $L1_0$ FePt films. The data in parentheses are taken from Ref [13]. In order to obtain the α^A_{xy}, the (θ_{AH}) values of 0.0056 and 0.030 are taken for FePd and FePt, respectively. The obtained θ_{AH} of FePd and FePt is consistent with previous works. [24,25,43]. For comparison, theoretical α^A_{xy}(int)/T values (calc.) are also listed. All the data here are taken at $T = 300$ K.

	S_{xx}	Q_s	S^A_{xy}	θ_{AN}	α^A_{xy}/T	α^A_{xy}(int)/T (calc.)
FePd	−25.768 (−19.85)	0.32 (0.40)	−0.408 (−0.468)	0.016 (0.024)	1.07 (1.84)	0.804
FePt	−17.688 (−12.31)	0.65 (0.55)	−0.821 (−0.698)	0.046 (0.057)	2.61 (2.94)	2.886

former term in Eq. (5) ($4\pi M_s Q_s/\rho_{xx}$). That is to say, the larger the Seebeck coefficient is, the smaller α^A_{xy} will be, which makes the curve of α^A_{xy}/T go flatter at small x, compared to the curve of Q_s. The key thermoelectric parameters are also derived from the data of Ref. [13], as shown in the parentheses of Table I. The α^A_{xy} shows evident decay from $L1_0$ FePt to $L1_0$ FePd in both the previous result and the current work, which is unlike the calculated ANC results predicted for the ordered alloys [10]. Nonetheless, to better understand the ANC in ordered alloys, we calculated and plotted the Pd-Pt site d-orbital spin-orbit coupling strength ξ_{PdPt} in Fig. 3(e). Interestingly, it shows that the experimentally derived α^A_{xy}/T and theoretical $\xi_{\mathrm{Pd\text{-}Pt}}$ both increase monotonically with Pt concentration x. The calculated $\xi_{\mathrm{Pt}} = 0.559$ eV, being almost three times larger than the calculated ξ_{Pd} of 0.194 eV, which is in good agreement with the ratio of α^A_{xy} (FePt)/α^A_{xy}(FePd). The results indicate that α^A_{xy} in $L1_0$ $FePd_{1-x}Pt_x$ is strongly related to the spin-orbit coupling of Pt-Pd atoms. However, the delivery from ξ to ANC is manifested through the change of Berry curvature. The detailed mechanism is further discussed in the next section.

C. Berry curvature and anomalous Nernst conductivity

The thermoelectric and transport measurements show that both α^A_{xy} and σ^A_{xy} in ordered $FePd_{1-x}Pt_x$ ternary alloys can be effectively tuned by the Pt-Pd chemical composition x. On the other hand, the calculated $\alpha^A_{xy}(\mathrm{int})/T$ at $T = 300$ K are $2.886 \times 10^{-3}\,\mathrm{Am^{-1}\,K^{-2}}$ and $0.804 \times 10^{-3}\,\mathrm{Am^{-1}\,K^{-2}}$ for FePt and FePd, respectively, and this follows the similar trend of the ANC obtained experimentally. First, the result indicates that thermoelectric conductivity can be well interpreted in terms of the Berry curvature, as the relativistic band structures of FePd and FePt are shown in Figs. 4(a) and 4(d). Figure 4(b) shows that from up to 0.4 eV above the E_F to down to -0.7 eV below the E_F, the $\sigma^A_{xy}(\mathrm{int})$ is positive and rather flat with small ripples in FePd. It is noted that at low temperatures, Eq. (8) can be simplified as the Mott relation [Eq. (6)] [7,21,29]. Thus, the $\alpha^A_{xy}(\mathrm{int})$ is approximately determined by the energy derivative (slope) of $\sigma^A_{xy}(\mathrm{int})$, which is expected to be small in FePd, leading to an insignificant ANC, as shown in Fig. 4(c). Meanwhile, the intrinsic AHC of FePt keeps increasing as the E_F changes from 0.4 to -0.7 eV, resulting in a very pronounced positive $\alpha^A_{xy}(\mathrm{int})$ as demonstrated in Figs. 4(e) and 4(f). The intrinsic AHC and ANC values for FePt are found to be $\sigma^A_{xy}(\mathrm{int}) = 830$ S/cm and $\alpha^A_{xy}(\mathrm{int}) = 0.8658\,\mathrm{Am^{-1}\,K^{-1}}$ (at $T = 300$ K), respectively. Examination of the calculated band-resolved Berry curvatures (not shown here) suggests that this large AHC arises predominantly from the large Ω_{xy} on the top valence band at the Γ point. Moreover, the difference in the ANC could

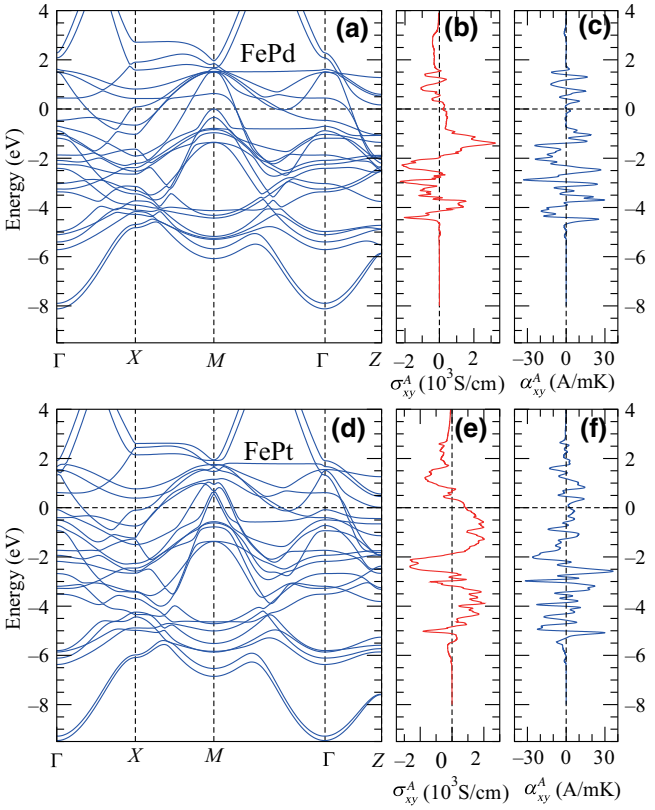

FIG. 4. Relativistic band structures of (a) FePd and (d) FePt; anomalous Hall conductivities of (b) FePd and (e) FePt as a function of energy; anomalous Nernst conductivities of (c) FePd and (f) FePt at $T = 300$ K as a function of energy. The Fermi level is at the zero energy.

be attributed to the larger SOC strength in the Pt atoms than in the Pd atoms, since the ξ dependence of the α^A_{xy} may reflect a strong difference in the distribution on the Berry curvature of FePt and FePd [24]. The $\alpha^A_{xy}(\mathrm{int})$ is simply given as the Brillouin zone integral of the Berry curvature on the Fermi surface. When the spin-orbit splitting occurs near the Fermi surface, very steep slope of the Berry curvature and the large $\alpha^A_{xy}(\mathrm{int})$ are induced. Secondly, it is worthy to note that the $\alpha^A_{xy}(\mathrm{int})/T$ of FePt (FePd) is slightly larger (smaller) than the experimentally acquired value. It might be attributed to the extrinsic scattering contributions due to lattice mismatch, defects, and impurities, which may change the total α^A_{xy} in experiments. The contributions to α^A_{xy}/T from impurity scattering are estimated to be 0.266×10^{-3} and $-0.276\times10^{-3}\,\mathrm{Am^{-1}\,K^{-2}}$ for FePd and FePt, respectively. The impurity induced ANC in FePt is of one order smaller than the intrinsic contributions, which is quite different from the results calculated previously [10]. The S^A_{xy}, Q_s and α^A_{xy} may change due to the distribution of impurity sites and the impurity density. In the previous calculated results, the extrinsic side-jump term of ANC contributes a large portion in total ANC in FePt and FePd.

Nonetheless, the magnitude of extrinsic ANC is larger than that of intrinsic ANC in FePd, leading to a comparable total ANC for FePd to that of FePt [10]. It is noted, for $L1_0$ Fe=Pt film grown on $Gd_3Ga_5O_{12}$ (GGG) substrate, the S^A_{xy} was reported to be much smaller than the current results [42]. Thus, it also leads to a small Q_s if the magnetization of FePt does not change much. The difference may be due to different substrates used to deposit the FePt film or may change because of the improved crystalline structure in $L1_0$-ordered alloys due to the annealing procedure.

Furthermore, the $\alpha^A_{xy}(\text{int})$ of both FePd and FePt as a function of temperature (T) is also calculated and the results are displayed in Fig. S1 within the Supplemental Material [19]. The magnitude of the ANC of FePt decreases steadily as T decreases, while it approaches zero at approximately 50 K. The magnitude for FePd also decreases monotonically with T, while it changes its sign at 125 K. The similar behavior is found in Fe, Mn_3Sn, and Mn_3Ge and requires further experimental evidence [10,29]. Nonetheless, the current result of ANC prompted us to calculate the spin Nernst conductivity (SNC) α^S_{xy} for FePt and FePd. Within the two-current model approximation, α^A_{xy} and α^S_{xy} can be written as $\alpha^A_{xy}(E) = \alpha^{\uparrow}_{xy}(E) + \alpha^{\downarrow}_{xy}(E)$, and $-(2e/\hbar)\alpha^S_{xy}(E) = \alpha^{\uparrow}_{xy}(E) - \alpha^{\downarrow}_{xy}(E)$, where $\alpha^{\uparrow}_{xy}$ and $\alpha^{\downarrow}_{xy}$ are the spin-up and spin-down Nernst conductivities, respectively [30]. The calculated values of α^S_{xy}/T are 0.697×10^{-3} and -0.958×10^{-3} $(\hbar/e)\,\text{Am}^{-1}\,\text{K}^{-2}$ for FePt and FePd at $T = 300$ K, respectively. Thus, our work provides evidence for a large intrinsic ANC of $L1_0$ FePt, and further suggests $L1_0$ FePd to achieve a large SNC, due to their band structures. Thus, the present results demonstrate $FePd_{1-x}Pt_x$ ordered alloys to be a very promising candidate for spin caloritronics applications such as thermo-spin valves and thermally driven spin-torque nanodevices.

IV. CONCLUSIONS

In summary, we experimentally determine the anomalous Nernst coefficient and anomalous Nernst conductivity in isoelectronic $L1_0$ $FePd_{1-x}Pt_x$ alloy films. We find that α^A_{xy} can be continuously tuned from 1.07×10^{-3} to $2.61 \times 10^{-3}\,\text{Am}^{-1}\text{K}^{-2}$, from $L1_0$ FePd to $L1_0$ FePt by increasing the Pt composition x. First-principles calculations show that the intrinsic ANC based on Berry curvature dominates the modification of the α^A_{xy}, when lighter Pd atoms are replaced by heavier Pt atoms. Our results will be helpful to better understand the various mechanisms of ANC in ferromagnetic alloys. By utilizing its high merit of sensitivity to the Fermi surface, ANE is expected to be a universal probe to investigate materials, such as the Weyl semimetals and chiral antiferromagnets [18,44]. Furthermore, the spin Nernst conductivity for $FePd_{1-x}Pt_x$ is also calculated, where a large α^S_{xy} can be achieved due to the large spin Nernst polarization in $L1_0$ FePd, which predicts a potential spin anomalous Nernst effect in the ordered alloys.

ACKNOWLEDGMENT

Z.S., S.J.X., and S.M.Z. are supported by the National Science Foundation of China (NSFC) with Grants No. 11774259, No. 51671147, No. 11874283, and the National Key R&D Program of China Grant No. 2017YFA0303202, the Fundamental Research Funds for the Central Universities. L.M. is supported by NSFC with Grant No. 51801152. G.Y.G. acknowledges the support from the Ministry of Science and Technology (107-2112-M-002-012-MY3) and Far Eastern Y. Z. Hsu Science and Technology Memorial Foundation in Taiwan.

[1] G. E. W. Bauer, E. Saitoh, and B. J. van Wees, Spin caloritronics, Nat. Mater. **11**, 391 (2012).
[2] H. Yu, S. D. Brechet, and J. P. Ansermet, Spin caloritronics, origin and outlook, Phys. Lett. A **381**, 825 (2017).
[3] S. R. Boona, R. C. Myers, and J. P. Heremans, Spin caloritronics, Energy Environ. Sci. **7**, 885 (2014).
[4] K. Uchida, S. Takahashi, K. Harii, J. Ieda, W. Koshibae, K. Ando, S. Maekawa, and E. Saitoh, Observation of the spin Seebeck effect, Nature **455**, 778 (2008).
[5] J. Flipse, F. K. Dejene, D. Wagenaar, G. E. W. Bauer, J. Ben Youssef, and B. J. van Wees, Observation of the Spin Peltier Effect for Magnetic Insulators, Phys. Rev. Lett. **113**, 027601 (2014).
[6] W.-L. Lee, S. Watauchi, V. L. Miller, R. J. Cava, and N. P. Ong, Anomalous Hall Heat Current and Nernst Effect in the $CuCr_2Se_{4-x}Br_x$ Ferromagnet, Phys. Rev. Lett. **93**, 226601 (2004).
[7] Y. Pu, D. Chiba, F. Matsukura, H. Ohno, and J. Shi, Mott Relation for Anomalous Hall and Nernst Effects in $Ga_{1-x}Mn_xAs$ Ferromagnetic Semiconductors, Phys. Rev. Lett. **101**, 117208 (2008).
[8] M. Mizuguchi, S. Ohata, K. Uchida, E. Saitoh, and K. Takanashi, Anomalous Nernst effect in an $L1_0$-ordered epitaxial FePt thin film, Appl. Phys. Express **5**, 093002 (2012).
[9] Y. Sakuraba, K. Hasegawa, M. Mizuguchi, T. Kubota, S. Mizukami, T. Miyazaki, and K. Takanashi, Anomalous Nernst effect in $L1_0$-FePt/MnGa thermopiles for new thermoelectric applications, Appl. Phys. Express **6**, 033003 (2013).
[10] J. Weischenberg, F. Freimuth, S. Blügel, and Y. Mokrousov, Scattering-independent anomalous Nernst effect in ferromagnets, Phys. Rev. B **87**, 060406(R) (2013).
[11] G. Y. Guo, Q. Niu, and N. Nagaosa, Anomalous Nernst and Hall effects in magnetized platinum and palladium, Phys. Rev. B **89**, 214406 (2014).
[12] K. Uchida, T. Kikkawa, T. Seki, T. Oyake, J. Shiomi, Z. Qiu, K. Takanashi, and E. Saitoh, Enhancement of anomalous Nernst effects in metallic multilayers free from proximity-induced magnetism, Phys. Rev. B **92**, 094414 (2015).

[13] K. Hasegawa, M. Mizuguchi, Y. Sakuraba, T. Kamada, T. Kojima, T. Kubota, S. Mizukami, T. Miyazaki, and K. Takanashi, Material dependence of anomalous Nernst effect in perpendicularly magnetized ordered-alloy thin films, Appl. Phys. Lett. **106**, 252405 (2015).

[14] X. Li, L. Xu, L. Ding, J. Wang, M. Shen, X. Lu, Z. Zhu, and K. Behnia, Anomalous Nernst and Righi-Leduc Effects in Mn_3Sn: Berry Curvature and Entropy Flow, Phys. Rev. Lett. **119**, 056601 (2017).

[15] M. Ikhlas, T. Tomita, T. Koretsune, M.-T. Suzuki, D. Nishio-Hamane, R. Arita, Y. Otani, and S. Nakatsuji, Large anomalous Nernst effect at room temperature in a chiral antiferromagnet, Nat. Phys. **13**, 1085 (2017).

[16] A. Sakai, Y. P. Mizuta, A. A. Nugroho, R. Sihombing, T. Koretsune, M.-T. Suzuki, N. Takemori, R. Ishii, D. Nishio-Hamane, R. Arita, P. Goswami, and S. Nakatsuji, Giant anomalous Nernst effect and quantum-critical scaling in a ferromagnetic semimetal, Nat. Phys. **14**, 1119 (2018).

[17] T. Seki, R. Iguchi, K. Takanashi, and K. Uchida, Relationship between anomalous Ettingshausen effect and anomalous Nernst effect in an FePt thin film, J. Phys. D: Appl. Phys., **51**, 254001 (2018).

[18] S. N. Guin, K. Manna, J. Noky, S. J. Watzman, C. Fu, N. Kumar, W. Schnelle, C. Shekhar, Y. Sun, J. Gooth, and C. Felser, Anomalous Nernst effect beyond the magnetization scaling relation in the ferromagnetic Heusler compound Co_2MnGa, NPG Asia Mater. **11**, 16 (2019).

[19] See Supplemental Material at http://link.aps.org/supplemental/10.1103/PhysRevApplied.13.054044 for details on the derivation of anomalous Nernst conductivity, procedures of anomalous Nernst effect measurement, and the temperature dependence of anomalous Nernst conductivity.

[20] D. Xiao, M.-C. Chang, and Q. Niu, Berry phase effects on electronic properties, Rev. Mod. Phys. **82**, 1959 (2010).

[21] N. F. Mott and H. Jones, *The Theory of the Properties of Metals and Alloys* (Dover, New York, 1958).

[22] Y. F. Ding, J. S. Chen, and E. Liu, Epitaxial $L1_0$ FePt films on SrTiO3 (100) by sputtering, J. Cryst. Growth. **276**, 111 (2005).

[23] J. S. Chen, B. C. Lim, Y. F. Ding, and G. M. Chow, Low-temperature deposition of $L1_0$ FePt films for ultra-high density magnetic recording, J. Magn. Magn. Mater. **303**, 309 (2006).

[24] P. He, L. Ma, Z. Shi, G. Y. Guo, J.-G. Zheng, Y. Xin, and S. M. Zhou, Chemical Composition Tuning of the Anomalous Hall Effect in Isoelectronic $L1_0$ $FePd_{1-x}Pt_x$ Alloy Films, Phys. Rev. Lett. **109**, 066402 (2012).

[25] K. M. Seemann, Y. Mokrousov, A. Aziz, J. Miguel, F. Kronast, W. Kuch, M. G. Blamire, A. T. Hindmarch, B. J. Hickey, I. Souza, and C. H. Marrows, Spin-Orbit Strength Driven Crossover between Intrinsic and Extrinsic Mechanisms of the Anomalous Hall Effect in the Epitaxial $L1_0$-Ordered Ferromagnets FePd and FePt, Phys. Rev. Lett. **104**, 076402 (2010).

[26] N. Nagaosa, J. Sinova, S. Onoda, A. H. MacDonald, and N. P. Ong, Anomalous Hall effect, Rev. Mod. Phys. **82**, 1539 (2010).

[27] H.-R. Fuh and G.-Y. Guo, Intrinsic anomalous Hall effect in nickel: A GGA + U study, Phys. Rev. B **84**, 144427 (2011).

[28] D. Xiao, Y. Yao, Z. Fang, and Q. Niu, Berry-Phase Effect in Anomalous Thermoelectric Transport, Phys. Rev. Lett. **97**, 026603 (2006).

[29] G.-Y. Guo and T.-C. Wang, Large anomalous Nernst and spin Nernst effects in the noncollinear antiferromagnets Mn_3X (X = Sn, Ge, Ga), Phys. Rev. B **96**, 224415 (2017); Phys. Rev. B **100**, 169907 (Erratum) (2019).

[30] J.-C. Tung and G.-Y. Guo, High spin polarization of the anomalous Hall current in Co-based Heusler compounds, New J. Phys. **15**, 033014 (2013).

[31] H.-L. Huang, J.-C. Tung, and G.-Y. Guo, Anomalous Hall effect and current spin polarization in Co_2FeX Heusler compounds (X = Al, Ga, In, Si, Ge, andSn): A systematic ab initio study, Phys. Rev. B **91**, 134409 (2015).

[32] T. Seki, S. Iihama, T. Taniguchi, and K. Takanashi, Large spin anomalous Hall effect in $L1_0$-FePt: Symmetry and magnetization switching, Phys. Rev. B **100**, 144427 (2019).

[33] S. Meyer, Y.-T. Chen, S. Wimmer, M. Althammer, T. Wimmer, R. Schlitz, S. Geprägs, H. Huebl, D. Ködderitzsch, H. Ebert, G. E. W. Bauer, R. Gross, and S. T. B. Goennenwein, Observation of the spin Nernst effect, Nat. Mater. **16**, 977 (2017).

[34] P. Sheng, Y. Sakuraba, Y.-C. Lau, S. Takahashi, S. Mitani, and M. Hayashi, The spin Nernst effect in tungsten, Sci. Adv. **3**, e1701503 (2017).

[35] G. Y. Guo, Y. Yao, and Q. Niu, *Ab initio* Calculation of the Intrinsic Spin Hall Effect in Semiconductors, Phys. Rev. Lett. **94**, 226601 (2005).

[36] G. Y. Guo and H. Ebert, Band-theoretical investigation of the magneto-optical Kerr effect in Fe and Co multilayers, Phys. Rev. B **51**, 12633 (1995).

[37] J. P. Perdew, K. Burke, and M. Ernzerhof, Generalized Gradient Approximation Made Simple, Phys. Rev. Lett. **77**, 3865 (1996).

[38] M. Chen, Z. Shi, W. J. Xu, X. X. Zhang, J. Du, and S. M. Zhou, Tuning anomalous Hall conductivity in L10 FePt films by long range chemical ordering, Appl. Phys. Lett. **98**, 082503 (2011).

[39] S. J. Pickart and R. Nathans, Alloys of the first transition series with Pd and Pt, J. Appl. Phys. **33**, 1336 (1962).

[40] J. W. Cable, E. O. Wollan, and W. C. Koehler, Distribution of magnetic moments in Pd $-$ 3d and Ni $-$ 3d alloys, Phys. Rev. **138**, A755 (1965).

[41] N. Cusack and P. Kendall, The absolute scale of thermoelectric power at high temperature, Proc. Phys. Soc. **72**, 898 (1958).

[42] T. Seki, K. Uchida, T. Kikkawa, Z. Qiu, E. Saitoh, and K. Takanashi, Observation of inverse spin Hall effect in ferromagnetic FePt alloys using spin Seebeck effect, Appl. Phys. Lett. **107**, 092401 (2015).

[43] Q. Hao, W. Chen, S. Wang, and G. Xiao, Anomalous Hall effect and magnetic properties of Fe_xPt_{100-x} alloys with strong spin-orbit interaction, J. Appl. Phys. **122**, 033901 (2017).

[44] H. Reichlova, R. Schlitz, S. Beckert, P. Swekis, A. Markou, Y.-C. Chen, D. Kriegner, S. Fabretti, G. Hyeon Park, A. Niemann, S. Sudheendra, A. Thomas, K. Nielsch, C. Felser, and S. T. B. Goennenwein, Large anomalous Nernst effect in thin films of the Weyl semimetal Co_2MnGa, Appl. Phys. Lett. **113**, 212405 (2018).

Correction: The previously published Figure 1 was processed incorrectly during production, resulting in the omission of red lines in parts (c) and (d) that indicate epitaxial growth. The entire figure has been replaced.